International Journal of Mechanical Sciences 133 (2017) 303–318

Contents lists available at ScienceDirect

International Journal of Mechanical Sciences

journal homepage: www.elsevier.com/locate/ijmecsci

Nonlinear dynamics of an adaptive origami-stent system

Guilherme V. Rodrigues[a], Larissa M. Fonseca[a], Marcelo A. Savi[a,*], Alberto Paiva[b]

[a] Center for Nonlinear Mechanics, COPPE – Department of Mechanical Engineering, Universidade Federal do Rio de Janeiro, 21.941.972 Rio de Janeiro, RJ, Brazil
[b] Department of Mechanical Engineering, Volta Redonda School of Engineering, Universidade Federal Fluminense, 27.255.250 Volta Redonda, RJ, Brazil

ARTICLE INFO

Keywords:
Origami
Adaptive structures
Shape memory alloys
Nonlinear dynamics
Chaos

ABSTRACT

Origami is an ancient art of the paper folding that has been the source of inspiration in many engineering designs due to its intrinsic ability of changing shape and volume. Self-expandable devices have been created based on origami concept together with smart materials. Shape memory alloys belong to this class of materials and provide high forces and large displacements by varying their temperature. This work deals with the nonlinear dynamics of an origami-stent, a cylindrical shaped origami structure, which has the capacity of changing its radius. The actuation is provided by antagonistic torsional shape memory alloy wires placed in the origami creases. The mathematical model assumes a polynomial constitutive model to describe the shape memory alloy thermomechanical behavior. Geometric assumptions establish a one-degree of freedom model with constitutive and geometric nonlinearities. Numerical simulations are carried out considering different thermomechanical loadings that represent operational conditions. The system presents complex responses including chaos.

1. Introduction

Origami, the art of the paper folding, has been inspiring many innovative designs of engineering systems. This Japanese art creates a three-dimensional geometry by following a sequence of folds in a sheet of paper. Some of these sequences creates a geometry able to contract-expand itself with an expressive change in its shape. Such behavior is of great interest to self-expanding adaptive systems.

The capacity of compacting structures, the lightness and the ability to present synchronized movements is of special interest of aerospace, robotic and medical applications [4,16]. In aerospace applications, the need and transportation restrictions motivate the use of packed configurations and, once arrived at the desired place, be deployed to the expanded configuration. Miura [15] developed a foldable solar panel based on origami concept. In medical applications, origami has inspired the design of new medical apparatus especially dedicated to minimally invasive surgery.

Shape memory alloys (SMAs) are widely employed as actuators due to their capacity of generate high forces and large displacements when subjected to thermomechanical fields that yield phase transformations. The association of SMA actuators with origami structures is promising being the focus of some research efforts [7,8,17]. Lee et al. [13] developed an origami-wheel actuated by SMA connected to a bias linear spring, being able to alter its radius in a robotic vehicle. The waterbomb pattern is employed for the origami design as employed on several applications since it allows significant shape changes [6,14]. Le et al. [12] also used a waterbomb origami pattern in an aerial drone employed to landing in water. Salerno et al. [18] presented an SMA origami device that takes advantage of geometric relations of the origami movements to increase the maneuver capacity.

Origami system is a slender structure with complex geometry that makes stability analysis an essential part of the design. Therefore, dynamical behavior of origami systems is an important issue to be investigated and only few works are available in literature. Basically, this analysis combines geometric and constitutive nonlinearities, providing a rich dynamics with operations close to the stability limits. In this regard, Fonseca et al. [5] presented a dynamical analysis of an origami-wheel with shape memory actuators. A single degree of freedom system is employed as an archetypal model of the origami structure. Results show a rich response, including chaos.

This work investigates the nonlinear dynamics of an origami-stent, a self-expandable cylindrical origami being originally presented by Kuribayashi et al. [11]. The stent is usually employed as a tubular medical device used to protect weakened arterial walls in the human body, but it can also be applied to increase stiffness of several systems including pipes and oil drilling well. Basically, origami-stent has a cylindrical shape and the folds allow the change of its radius (Fig. 1).

A shape memory alloy origami-stent system is analyzed considering torsion SMA wires (TSW) as actuators. A polynomial constitutive model describes thermomechanical behavior of SMAs. Origami geometric relations are employed to propose a one-degree of freedom (1-DOF) system

* Corresponding author.
E-mail addresses: guilherme_@live.co.uk (G.V. Rodrigues), larissamaciel.lah@gmail.com (L.M. Fonseca), savi@mecanica.ufrj.br (M.A. Savi), paiva.ufrj@gmail.com (A. Paiva).

http://dx.doi.org/10.1016/j.ijmecsci.2017.08.050
Received 6 April 2017; Received in revised form 20 August 2017; Accepted 26 August 2017
Available online 1 September 2017
0020-7403/

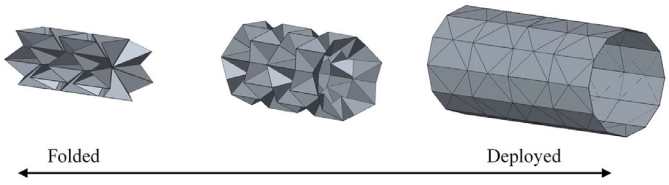

Fig. 1. Origami-stent deployment: three different configurations from folded, closed one, to deployed, opened one.

that represents the system dynamics. Numerical simulations are carried out showing rich responses due to situations related to different thermomechanical operational excitations.

After this introduction, this paper is organized as follows. Initially, a geometric analysis is performed, establishing geometric relations and the kinematics of the origami system. Dynamical model is then proposed considering a single-degree of freedom system. Afterward, numerical simulations are discussed considering different thermal and thermomechanical loadings. Concluding remarks are presented in the sequence.

2. Geometric analysis

The origami-stent is a self-expandable cylindrical origami constructed by following the folding pattern showed in Fig. 2-a, where the continuous lines mean mountain folds (folds outwards the paper plane) and the dashed lines mean valley folds (folds inwards the paper plane). This pattern is composed by the repetition of rectangular components as showed in Fig. 2-b, which is known as waterbomb base, shifted half an element in comparison with those on their side. The rectangular element has a length L and an angle α_0, and therefore, $L_2 = L/\tan(\alpha_0)$ and $\alpha_0 = 45^\circ$ means it is a square element. A single waterbomb base folded is presented in Fig. 2-c.

Geometric relations are now in focus and some hypotheses are established for this aim. The first one is the symmetry, assuming that all elements behave in the same way and the element itself behaves symmetrically. Under this assumption, one-quarter of the cell element is representative of the general cell behavior. The second assumption is that fold occurs only in the creases and therefore, the element facets remain straight. Under these assumptions, it is possible to analyze the whole origami from a single cell element.

The deployment of the origami goes through two stages [10]. On the first stage, the element unfolds until it reaches a flattened configuration and the nodes A, C and A_2 are co-linear. On the second stage, the crease AA_2 moves outwards in the radial direction (Fig. 3).

The cell element geometry is characterized by three angles: θ, φ and β. These angles are coupled in such a way that each one can be described as a function of the others. Hence, it is possible to elect θ as the basic angle. It is noticeable that $\theta < 90^\circ$ characterizes the first stage while $\theta > 90^\circ$ characterizes the second stage.

On the first stage, φ can be expressed by considering the positions of the points A and B on the (x,y,z) system with origin on C: $A = (L_2\sin(\varphi),0, L_2\cos(\varphi))$ and $B = (L_2, L\sin(\theta), L\cos(\theta))$. Since the distance AB is equal to L, the following equation can be written:

$$\cos(\alpha_0) = \cos(\alpha_0)\sin(\varphi) + \sin(\alpha_0)\cos(\varphi)\cos(\theta) \tag{1}$$

By solving Eq. (1), the following equation is obtained:

$$\left(\sin(\varphi) - \frac{1-\tan^2(\alpha_0)\cos^2(\theta)}{1+\tan^2(\alpha_0)\cos^2(\theta)}\right)(\sin(\varphi)-1) = 0 \tag{2}$$

Based on that, there are two possible solutions for φ. Since this angle cannot be constant on the first stage, the following equation is established to define φ during the first stage:

$$\varphi = \operatorname{asin}\left(\frac{1-\tan^2(\alpha_0)\cos^2(\theta)}{1+\tan^2(\alpha_0)\cos^2(\theta)}\right) \tag{3}$$

In order to analyze the angle β on the first stage, consider the triangle A_pB_pC (Fig. 4). Since $A_pC = L_2\cos(\varphi)$ and $D_pC = L\cos(\theta)$, it is possible to write $A_pD_p = L_2\cos(\varphi) - L\cos(\theta)$. On the other hand, $AD = L\cos(\beta)$ and, since the angle $\angle ADD_p = \varphi$, the distance $A_pD_p = L\cos(\beta)\sin(\varphi)$. Therefore, the following relation is written for the first stage:

$$\beta = \operatorname{acos}\left(\frac{\cos(\varphi)/\tan(\alpha_0) - \cos(\theta)}{\sin(\varphi)}\right) \tag{4}$$

In order to obtain a function of β that depends only of θ, the angle φ in Eq. (4) is substituted by Eq. (3) and it is found that $\beta = \operatorname{acos}(\cos(\theta)) = \theta$.

On the second stage, Fig. 3 shows that the angle φ remains constant, being equal to 90°. This can be also pointed out by considering the second term on the left side of Eq. (2). Besides, since both facets that contains the crease BC remains on the same plane, $\beta = 180^\circ - \theta$.

An analysis of the origami-stent radii is now of concern. Let O be the central point of the origami-stent. Fig. 5 shows two radii that define origami geometry: an internal radius, R_i, defined as OC; and an external radius, R_e, defined as OB_p. The angle α, defined as $\angle A_pOB_p$, is related to the number of cell elements circumferentially distributed, n, and by the hypotheses already assumed, it is equal to all elements. Therefore, this angle is such that $n(2\alpha) = 360^\circ$. Hence:

$$\alpha = 180^\circ/n \tag{5}$$

Reminding that θ is the angle $\angle A_pCB_p$, it is possible to see from Fig. 5 that $R_e\sin(\alpha) = L\sin(\theta)$ and $R_e\cos(\alpha) = R_i + L\cos(\theta)$, furnishing the following relations:

$$R_e = \frac{L\sin(\theta)}{\sin(\alpha)} \tag{6}$$

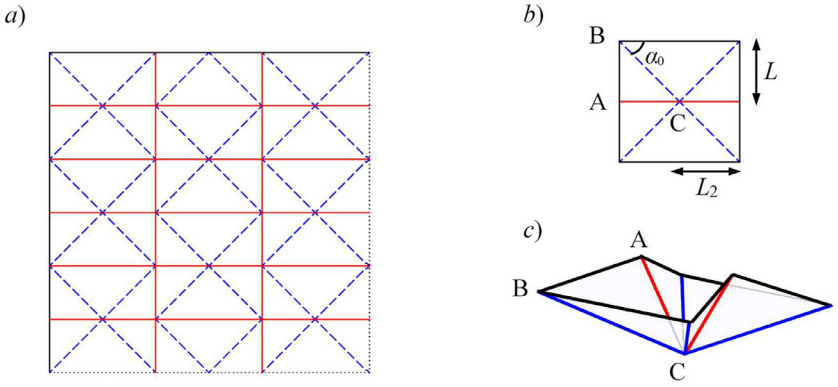

Fig. 2. Origami-stent folding pattern: (a) waterbomb folding pattern where continuous line represents mountains and dashed line represents valleys; (b) plane view of the single cell element; (c) three-dimensional view of the single cell element.

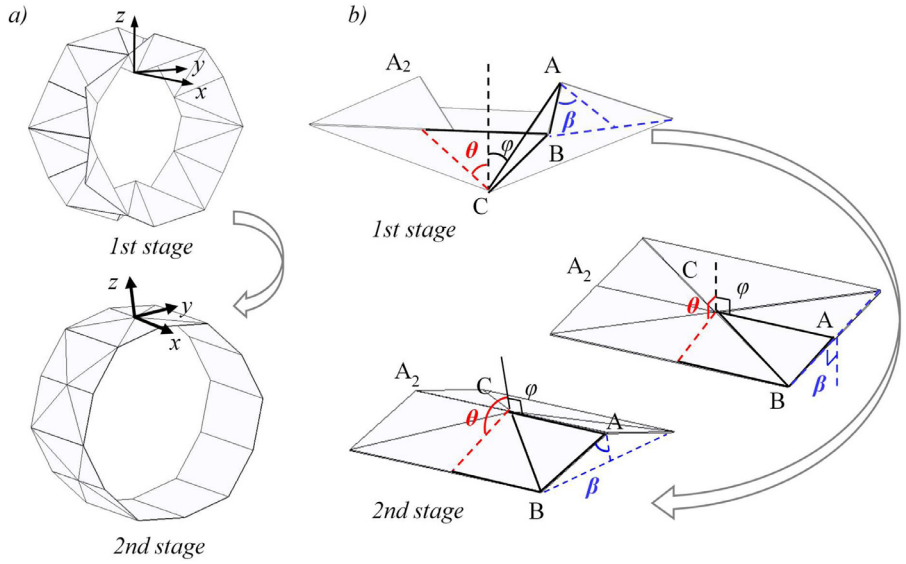

Fig. 3. Origami-stent two-stage configurations: (a) row of elements; (b) single element.

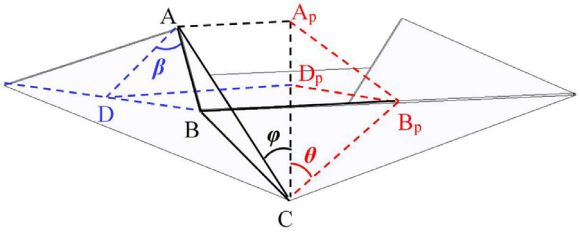

Fig. 4. Geometric characterization using angles of the origami-stent single element.

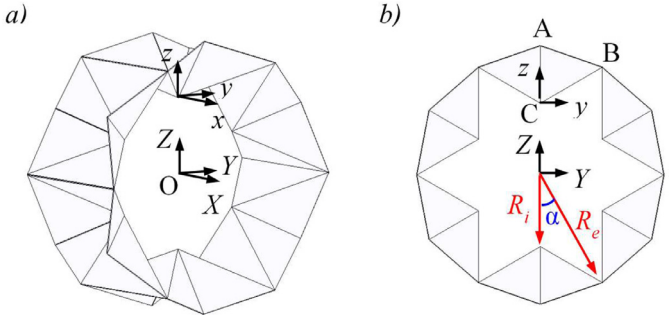

Fig. 5. Geometric characterization using internal and external radii of the origami-stent: (a) perspective view; (b) frontal view.

$$R_i = \frac{L\sin(\theta)}{\tan(\alpha)} - L\cos(\theta) \tag{7}$$

The origami has physical limitations that can be expressed as follows: the radius R_i cannot be less than zero, which means that the structure does not penetrate itself; R_i cannot be greater than R_e, which means that the mountain AC does not become a valley avoiding a fold in another direction that would result in the structure collapse. Hence, $R_i = 0$ implies that $\tan(\theta) = \tan(\alpha)$ and $R_i = R_e$ implies that $\tan(\theta) = \sin(\alpha)/(\cos(\alpha) - 1)$. These restrictions can be written by the definition of limit angles, $\theta_{\min}$ and $\theta_{\max}$:

$$\theta_{\min} = \alpha \tag{8}$$

$$\theta_{\max} = \frac{\pi}{2} + \frac{\alpha}{2} \tag{9}$$

In summary, the origami geometry can be described with the following set of equations:

$$\beta = \begin{cases} \theta & \text{if } \theta_{\min} \le \theta < 90° \\ 180° - \theta & \text{if } 90° \le \theta \le \theta_{\max} \end{cases} \tag{10}$$

$$\varphi = \begin{cases} \operatorname{asin}\left(\dfrac{1 - \tan^2(\alpha_0)\cos^2(\theta)}{1 + \tan^2(\alpha_0)\cos^2(\theta)}\right) & \text{if } \theta_{\min} \le \theta < 90° \\ 90° & \text{if } 90° \le \theta \le \theta_{\max} \end{cases} \tag{11}$$

Based on the geometric relations of the origami-stent, Fig. 6 illustrates the general behavior of an origami with square elements ($\alpha_0 = 45°$). Fig. 6-a shows the evolution of the angles β and φ as a function of the angle θ. Note that at $\theta = 90°$, both angles (β and φ) have a transition configuration between the different stages. Fig. 6-b shows internal and external radii divided by the length L for different values of n (the number of elements circumferentially distributed). Besides the limit angles, $\theta_{\min}$ and $\theta_{\max}$, the number n influences the radius maximum values. The maximum value of the external radius R_e occurs at $\theta = 90°$. Fig. 6-b also shows the degree of compactness of the structure. For $n = 6$, R_e can double its size, while for $n = 10$, R_e can triplicate its size. Hence, the greater is the value of elements n, the more compact the origami is able to be. Nevertheless, the increase of the number of elements makes harder the origami manufacturing process.

2.1. Kinematic analysis

Kinematics of the origami-stent system is now treated. Due to symmetry assumptions, it is possible to analyze one-quarter of the cell element. A global coordinate frame F(*OXYZ*) is placed on the center axis of the origami-stent with origin on O (see Fig. 5). A local coordinate frame P(C*xyz*) is placed due to a translation from O to C (see Fig. 5). Hence, the coordinate frame P is translated from the coordinate frame F through *Z* direction of a distance equal to OC, that is, R_i.

Basically, kinematic analysis corresponds to two triangles which movements are geometrically coupled to each other. It is assumed that each one of these triangles rotates presenting inertia. The triangle BB_pC rotates of an angle θ while the triangle ABC rotates of an angle φ and then of an angle β (see Fig. 4). Besides that, translation motion associated with each triangle has a lumped mass placed in its centroid: m_1 on the centroid of the triangle ABC and m_2 on the centroid of the triangle BB_pC.

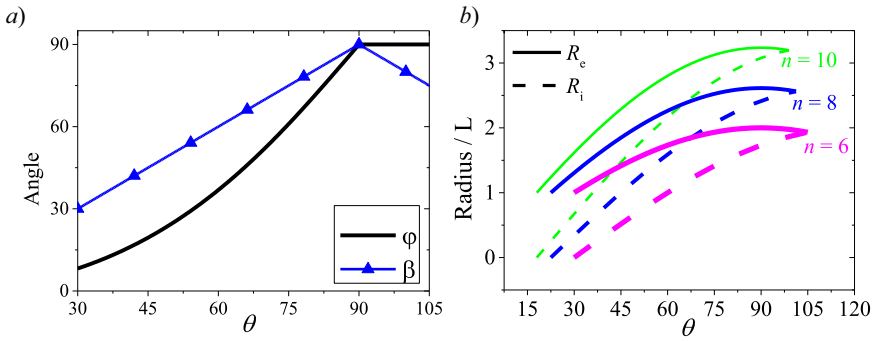

Fig. 6. Geometric relations defined by origami angles and radius as a function of θ (in degrees for $\alpha_0 = 45°$): (a) angle relations (β and φ); (b) radius relations (R_i and R_e) for different values of n.

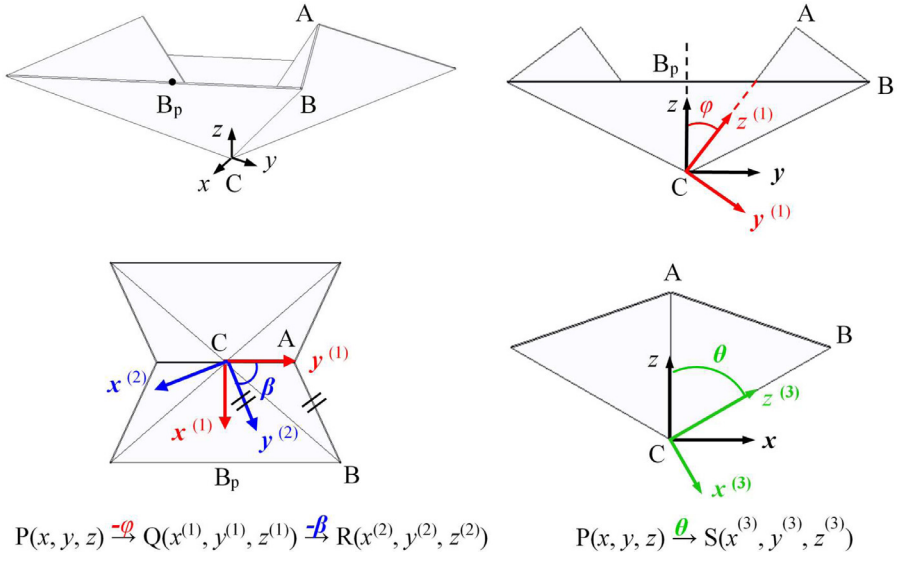

Fig. 7. Coordinate frames defined on the origami-stent single element.

Therefore, five coordinate frames are considered: F and P; Q, R and S. The coordinate frames Q, R and S have origin on C, presenting movements related to each geometric angle, φ, β and θ, respectively (Fig. 7). The triangle ABC rotates about φ and, then, rotates about β. Q(C$x^{(1)}y^{(1)}z^{(1)}$) rotates about φ in the $x^{(1)}$-axis direction of P while R(C$x^{(2)}y^{(2)}z^{(2)}$) rotates about β in the $z^{(2)}$-axis direction of Q. The triangle BB_pC rotates θ. S(C$x^{(3)}y^{(3)}z^{(3)}$) rotates about θ on the $y^{(3)}$-axis of P. Since the coordinate frame P does not rotates about the global coordinate frame F (it only translates), the rotation matrices are the following:

$$ {}^{F}\boldsymbol{T}^{\boldsymbol{Q}} = \begin{bmatrix} 1 & 0 & 0 \\ 0 & \cos(\varphi) & \sin(\varphi) \\ 0 & -\sin(\varphi) & \cos(\varphi) \end{bmatrix} \tag{12} $$

$$ {}^{\boldsymbol{Q}}\boldsymbol{T}^{\boldsymbol{R}} = \begin{bmatrix} \cos(\beta) & \sin(\beta) & 0 \\ -\sin(\beta) & \cos(\beta) & 0 \\ 0 & 0 & 1 \end{bmatrix} \tag{13} $$

$$ {}^{F}\boldsymbol{T}^{\boldsymbol{S}} = \begin{bmatrix} \cos(\theta) & 0 & \sin(\theta) \\ 0 & 1 & 0 \\ -\sin(\theta) & 0 & \cos(\theta) \end{bmatrix} \tag{14} $$

It is assumed that the lumped masses m_1 and m_2 are located in the geometric center of the triangles ABC and BB_pC, respectively. The vectors that indicate their positions are represented on the coordinate frames R and S, respectively, given by:

$$ {}^{\boldsymbol{R}}_{\boldsymbol{C}}\boldsymbol{r}_1 = \begin{bmatrix} 0 \\ L_1/3 \\ 2L_2/3 \end{bmatrix} \tag{15} $$

$$ {}^{\boldsymbol{S}}_{\boldsymbol{C}}\boldsymbol{r}_2 = \begin{bmatrix} 0 \\ L_2/3 \\ 2L_1/3 \end{bmatrix} \tag{16} $$

The triangle inertia tensors are the following:

$$ {}^{\boldsymbol{R}}\boldsymbol{I}_{ABC} = m_{ABC}\begin{bmatrix} \frac{1}{6}{L_1}^2 + \frac{1}{2}{L_2}^2 & 0 & 0 \\ 0 & \frac{1}{2}{L_2}^2 & -\frac{1}{4}L_1L_2 \\ 0 & -\frac{1}{4}L_1L_2 & \frac{1}{6}{L_1}^2 \end{bmatrix} \tag{17} $$

$$ {}^{\boldsymbol{S}}\boldsymbol{I}_{BBpC} = m_{BBpC}\begin{bmatrix} \frac{1}{6}{L_2}^2 + \frac{1}{2}{L_1}^2 & 0 & 0 \\ 0 & \frac{1}{2}{L_1}^2 & -\frac{1}{4}L_1L_2 \\ 0 & -\frac{1}{4}L_1L_2 & \frac{1}{6}{L_2}^2 \end{bmatrix} \tag{18} $$

After these definitions, it is defined triangle angular velocities with respect to the global frame:

$$ {}^{F}\boldsymbol{\omega}_{ABC} = \begin{bmatrix} \dot{\varphi} \\ \sin(\varphi)\dot{\beta} \\ \cos(\varphi)\dot{\beta} \end{bmatrix} \tag{19} $$

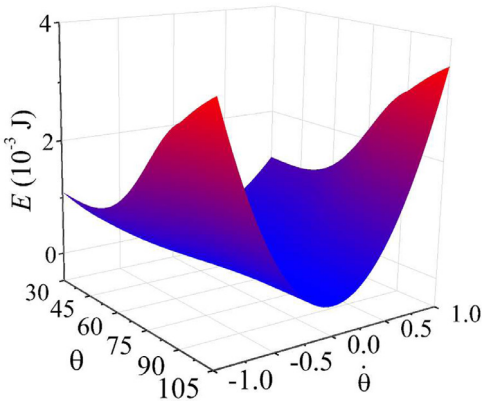

Fig. 8. Kinetic energy of origami-stent square element with unitary length and unitary masses and six elements ($n=6$).

$$ {}^{F}\boldsymbol{\omega}_{BBpC} = \begin{bmatrix} 0 \\ \dot{\theta} \\ 0 \end{bmatrix} \tag{20} $$

The lumped mass linear velocities $\boldsymbol{v}_1$ and $\boldsymbol{v}_2$ are given by the position time derivative, reminding that all angles are described as a function of $\theta=\theta(t)$.

$$ {}^{F}\boldsymbol{v}_1 = \frac{d}{dt}\left[{}^{F}\boldsymbol{T}^{QQ}\boldsymbol{T}^{RR}_{C}\boldsymbol{r}_1\right] = \\ = \begin{bmatrix} \frac{1}{3}L_1\cos(\beta)\dot{\beta} \\ -\frac{1}{3}L_1\sin(\beta)\cos(\varphi)\dot{\beta} - \left(\frac{1}{3}L_1\cos(\beta)\sin(\varphi) - \frac{2}{3}L_2\cos(\varphi)\right)\dot{\varphi} \\ +\frac{1}{3}L_1\sin(\beta)\sin(\varphi)\dot{\beta} - \left(\frac{1}{3}L_1\cos(\beta)\cos(\varphi) + \frac{2}{3}L_2\sin(\varphi)\right)\dot{\varphi} + \dot{R}_i \end{bmatrix} \tag{21} $$

$$ {}^{F}\boldsymbol{v}_2 = \frac{d}{dt}\left[{}^{F}\boldsymbol{T}^{SS}_{C}\boldsymbol{r}_2\right] = \begin{bmatrix} \frac{2}{3}L_1\cos(\theta)\dot{\theta} \\ 0 \\ -\frac{2}{3}L_1\sin(\theta)\dot{\theta} + \dot{R}_i \end{bmatrix} \tag{22} $$

3. Dynamical model

The dynamical analysis of the origami-stent system assumes kinematic relations in order to write an equivalent 1-DOF system to represent the origami dynamics. Equations of motion are formulated by considering energetic approach, electing angle θ as a generalized coordinate. Using the transformation matrices to describe all terms in the system F, the kinetic energy E is given by:

$$ E = \frac{1}{2}m_1{}^{F}\boldsymbol{v}_1\cdot{}^{F}\boldsymbol{v}_1 + \frac{1}{2}m_2{}^{F}\boldsymbol{v}_2\cdot{}^{F}\boldsymbol{v}_2 + \frac{1}{2}\left({}^{F}\boldsymbol{\omega}_{ABC}\right)^{T}{}^{F}\boldsymbol{I}_{ABC}{}^{F}\boldsymbol{\omega}_{ABC} + \\ + \frac{1}{2}\left({}^{F}\boldsymbol{\omega}_{BBpC}\right)^{T}{}^{F}\boldsymbol{I}_{BBpC}{}^{F}\boldsymbol{\omega}_{BBpC} \tag{23} $$

Fig. 8 shows the kinetic energy E as a function of θ and its time derivative, $\dot{\theta}$, for a square element, considering $n=6$, unitary length L and unitary masses. Fig. 9 shows the projection of this energy for different values of n, in the left as a function of $\dot{\theta}$ for $\theta=90^\circ$ and in the right as function of θ for a unitary velocity ($\dot{\theta}=1/s$). It should be pointed out that the energy is a nonsmooth function at $\theta=90^\circ$ due to changes of the angles β and φ (see Fig. 6).

The actuation of the origami-stent is provided by a Torsion SMA Wire (TSW) with length L_S and radius r_S [9]. Two TSWs are antagonistically placed on each side of a cell element on the crease AC (Fig. 10) and these actuators promote the origami configuration changes (opening and closing).

The SMA thermomechanical behavior is described by a polynomial constitutive model [3,19] that establishes a stress-strain-temperature ($\sigma-\gamma-T$) relation. This constitutive model considers that the austenitic phase is stable at high temperatures, and two variants of the martensitic phase, induced by positive and negative stress fields, stable at low temperatures.

$$ \sigma = a_1\left(T-T_M\right)\gamma - a_2\gamma^3 + a_3\gamma^5 \tag{24} $$

where a_1, a_2 and a_3 are material parameters and T_M is the temperature below which the martensitic phase is stable. By considering T_A as the temperature above which the austenitic phase is stable, it is possible to write the following relationship: $a_3 = \frac{1}{4}\frac{a_2^2}{a_3(T_A-T_M)}$.

Aguiar et al. [1] and Enemark et al. [2] showed that helical spring force-displacement-temperature curve is similar to the stress-strain-temperature curve assuming homogeneous phase transformation through the spring element. Under this assumption, it is possible to use the same argues to define an torsional actuator torque-displacement-temperature relation that is formally similar to the stress-strain-temperature:

$$ M = \frac{J}{r_s}\left[a_1\left(T-T_M\right)\left(2\frac{r_s}{L_s}\theta - 2\frac{r_s}{L_s}\theta_I\right) \right. \\ \left. -a_2\left(2\frac{r_s}{L_s}\theta - 2\frac{r_s}{L_s}\theta_I\right)^3 + a_3\left(2\frac{r_s}{L_s}\theta - 2\frac{r_s}{L_s}\theta_I\right)^5\right] \tag{25} $$

where θ_I is the angle where the TSW is free of stress. Note that this expression represents constitutive relation of both actuators, being expressed by $M_{TSW\,1}$ and $M_{TSW\,2}$.

On the origami-stent system, the generalized forces Q_θ are related to the TSW generalized force M_{SMA}, which due to symmetric considerations is given by: $M_{SMA}=(M_{TSW\,1}+M_{TSW\,2})/2$. An external generalized force Q_{ext} is applied at the point C, z-direction. Hence, the expression of the virtual work δW, neglecting gravitational effect, is given by:

$$ \delta W = Q_\theta\delta\theta = -M_{SMA}(\theta)\delta\theta + Q_{ext}\delta R_i \tag{26} $$

Note that $R_i=R_i(\theta)$, $\delta R_i=\partial R_i/\partial\theta\delta\theta$, and therefore, $Q_\theta=-M_{SMA}(\theta)+Q_{ext}\partial R_i/\partial\theta$. Two extra generalized forces are considered in order to have a complete description of the origami-stent system. The first one is related to a linear viscous dissipation of coefficient ζ representing all dissipation processes, including the hysteresis phenomenon: $\delta W_D=\zeta\dot{\theta}\delta\theta$. The second one is related to origami geometric restrictions that limit θ to vary in the range $[\theta_{\min},\theta_{\max}]$ Eqs. (8) and (9), expressed as a moment of the form:

$$ M_{lim}(\theta) = \begin{cases} k_{lim}\left(\theta-\theta_{min}\right) & , \text{ if } \theta<\theta_{min} \\ 0 & , \text{ if } \theta_{min}\le\theta\le\theta_{max} \\ k_{lim}\left(\theta-\theta_{max}\right) & , \text{ if } \theta>\theta_{max} \end{cases} \tag{27} $$

where k_{lim} limits the system response and represents an equivalent elastic spring stiffness.

Equation of motion is then obtained from Lagrange's equation.

$$ \frac{\partial}{\partial t}\left(\frac{\partial E}{\partial\dot{\theta}}\right) - \left(\frac{\partial E}{\partial\theta}\right) = Q_\theta = -\zeta\dot{\theta} - M_{SMA}(\theta) - M_{lim}(\theta) + Q_{ext}\frac{\partial R_i}{\partial\theta} \tag{28} $$

The kinetic energy (23) is a nonlinear expression in θ multiplied by the velocity and can be written as $E=g(\theta)\dot{\theta}^2$. Details about this function are presented in Appendix. Substituting this expression in the left hand side of Lagrange's Eq. (28), it gives a term $g_1(\theta)\ddot{\theta}$ and a term $g_2(\theta)\dot{\theta}^2$ (see Appendix for more details). Therefore, the equation of motion is written as follows:

$$ g_1(\theta)\ddot{\theta} + g_2(\theta)\dot{\theta}^2 = -\zeta\dot{\theta} - M_{SMA}(\theta) - M_{lim}(\theta) + Q_{ext}\frac{\partial R_i}{\partial\theta} \tag{29} $$

In order to write dimensionless equations, it is defined a dimensionless time $\tau=\omega_{REF}t$, where ω_{REF} is a reference frequency, defined from the linear part of the restitution force:

$$ \omega_{REF} = \sqrt{\frac{Ja_1T_M}{m_1L^2L_S}} \tag{30} $$

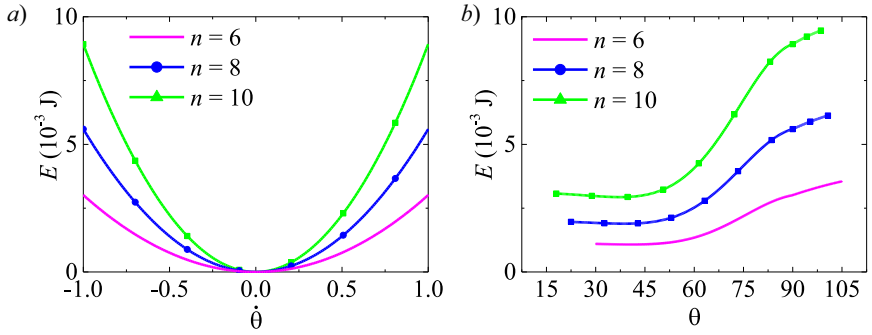

Fig. 9. Projections of the kinetic energy of origami-stent square element with unitary length and unitary masses for different number of elements, n; (a) $\theta = 90^{\circ}$; (b) $\dot{\theta} = 1/s$.

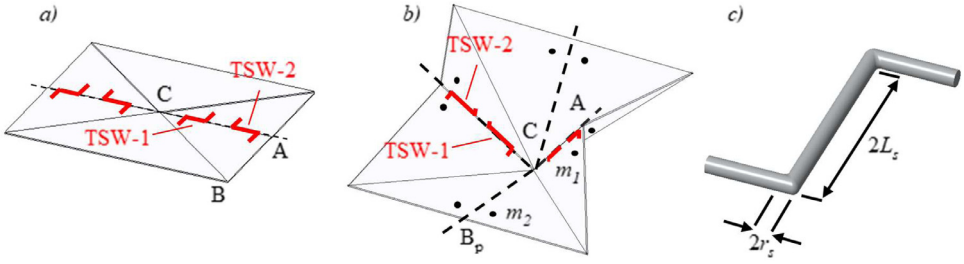

Fig. 10. Actuation system provided by Torsion Spring Wires (TSWs): (a) the placement of the actuators at the planar single element; (b) a folded single element with TSWs and lumped masses placed on the triangles' centroids; (c) Torsional Spring Wire (TSW).

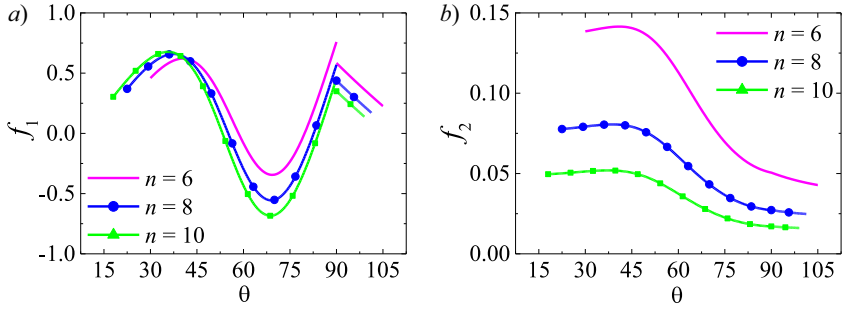

Fig. 11. Dimensionless functions $f_1(\theta)$ and $f_2(\theta)$ that define geometrical nonlinearities of the dynamical model ($\alpha_0 = 45^{\circ}$).

Hence, after dividing Eq. (29) by $m_1 L^2 {\omega_{REF}}^2$, the following set of equations of motion is written:

$$\begin{cases} \theta' = v \\ \theta'' = -f_1(\theta)v^2 - f_2(\theta)\xi v - f_2(\theta)H_M(\theta) + f_2(\theta)\left(\frac{1}{L}\frac{\partial R_i}{\partial \theta}\right)D_{ext} \end{cases} \tag{31}$$

where $(\,)' = \partial()/\partial\tau$, and therefore $\dot{\theta} = \theta' \omega_{REF}$ and $\ddot{\theta} = \theta'' {\omega_{REF}}^2$. Besides, the following dimensionless terms are employed:

$$f_1(\theta) = \frac{g_2(\theta)}{g_1(\theta)} \tag{32}$$

$$f_2(\theta) = \frac{m_1 L^2}{g_1(\theta)} \tag{33}$$

$$H_M = \frac{M_{SMA}(\theta) + M_{lim}(\theta)}{m_1 L^2 {\omega_{REF}}^2} \tag{34}$$

$$D_{ext} = \frac{Q_{ext}}{m_1 L {\omega_{REF}}^2} \tag{35}$$

$$\xi = \frac{\zeta}{m_1 L^2 \omega_{REF}} \tag{36}$$

Fig. 11 presents dimensionless functions $f_1(\theta)$ and $f_2(\theta)$ for a square element and equal masses. The discontinuity of the function $f_1(\theta)$ at $\theta = 90^{\circ}$ is due to the nonsmoothness of the kinetic energy. These functions indicate the origami-stent nonlinearities.

4. Numerical simulations

Dynamical behavior of the origami-stent system actuated by two antagonistic TSWs is now analyzed. Numerical simulations are carried out by employing the fourth-order Runge–Kutta method. Different thermal and thermomechanical loads are contemplated to study the system behavior under distinct operational conditions.

Table 1 presents the origami-stent parameters employed in all simulations considering a square element. Besides, a dissipation coefficient $\xi = 0.3$ is employed. Under these conditions, the reference frequency is $\omega_{REF} = 62.09\ rad/s$. Temperature T_0 represents a reference temperature where the origami-stent actuator does not apply any moment at a chosen angle of $\theta = 30^{\circ}$ (closed configuration). Thereby, one actuator has $\theta_I = 30^{\circ}$ The other one has $\theta_I = 90^{\circ}$ since this assures that the origami can reach the opened configuration of maximum radius ($\theta = 90^{\circ}$) by changing the TSW temperature. This set of parameters can represent a human body stent. Note that the length L of the cell element is 6.6 mm. Hence, for $n = 6$, the external radius $R_e = 13.2$ mm for $\theta = 90^{\circ}$ (Eq. (6)), which is close to the usual radius of aortal stent grafts.

Fig. 12 presents the torque of the TSWs as a function of θ at the temperature T_0 and at $T = 310K$ ($T > T_A$). TSW-1 is located at $\theta_I = 90^{\circ}$ with a temperature T_1 while TSW-2 is at $\theta_I = 30^{\circ}$ with a temperature T_2.

Table 1
Origami-stent parameters.

$m_1 = m_2$ (kg)	$m_{ABC} = m_{BBpC}$ (kg)	L (m)	r_s (m)	L_s (m)	k_{lim} (N m)
5×10^{-5}	5×10^{-5}	6.6×10^{-3}	8.0×10^{-5}	2.2×10^{-3}	1.0×10^{-2}
a_1 (MPa/K)	a_2 (MPa)	a_3 (MPa)	T_M (K)	T_A (K)	T_0 (K)
1.0×10^{6}	$1.4\times101^{\circ}$	2.2×101^{2}	287.15	309.1	293.15

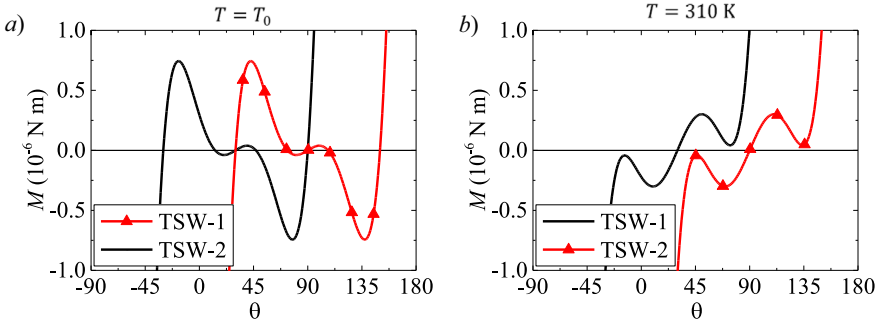

Fig. 12. Torque of the TSWs at different temperatures: (a) reference temperature T_0; (b) $T = 310$ K.

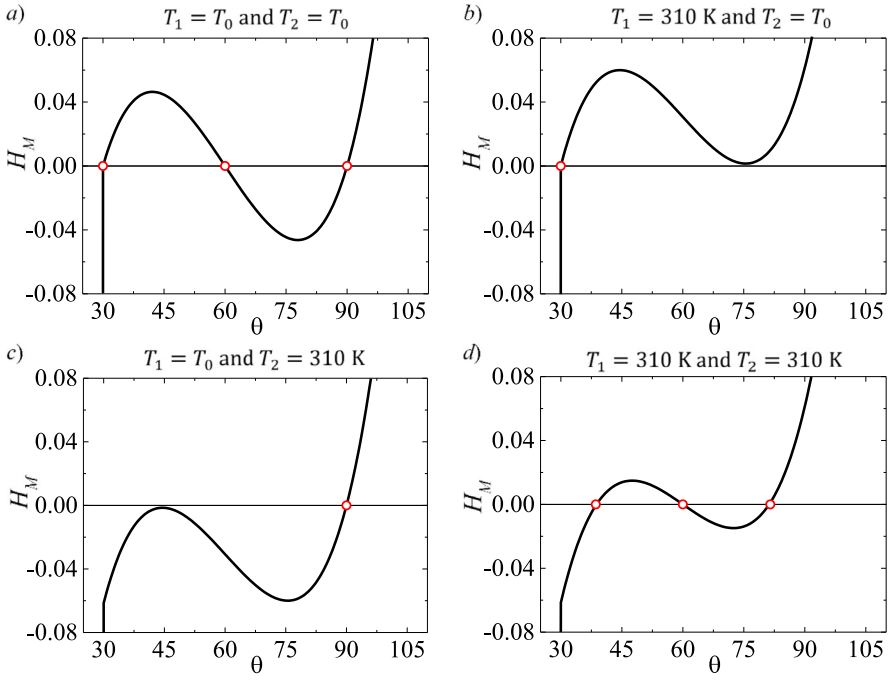

Fig. 13. Actuator temperature influence on the generalized forces: (a) TSW-1 and TSW-2 at reference temperature with three vanishing points; (b) TSW-1 at high temperature with one vanishing point at 30°; (c) TSW-2 at high temperature with one vanishing point at 90°; (d) TSW-1 and TSW-2 at high temperature with three vanishing points.

Concerning external excitation, a harmonic external force is considered of amplitude μ and frequency Ω.

$$D_{ext} = \mu \sin(\Omega\tau) \tag{37}$$

In addition, temperature has fluctuations represented by:

$$T = T_f + \mu_T \sin(\Omega_T \tau) \tag{38}$$

where T_f is the temperature around which the temperature T oscillates.

4.1. Thermal loadings

The actuator temperature influence on the system dynamical response is investigated considering different thermal loadings. An overview of the origami-stent equilibrium configurations can be provided by the analysis of the moments represented by H_M (Eq. (34)). Fig. 13 presents these moments for different pairs of temperatures and $n = 6$. In the reference configuration (Fig. 13-a), $T_1 = T_2 = T_0$, the sum of the moments vanishes at three angles: 30°, 60° and 90° If the temperature T_1 is greater than T_A ($T_1 = 310$ K) while $T_2 = T_0$, only 30° is an equilibrium point (Fig. 13-b). On the other hand, if the temperature T_2 is greater than T_A ($T_2 = 310$ K) while $T_1 = T_0$, only 90° is an equilibrium point (Fig. 13-c). If the temperatures of both TSWs are greater than T_A ($T_1 = T_2 = 310$ K), there are again three points where the sum of the moments is zero (Fig. 13-d). Therefore, by controlling the temperature one can establish the configuration (opened or closed) of the origami-stent, defining the equilibrium point structure.

Free vibration analysis is now of concern identifying the temperature influence. Figs. 14 and 15 present the dynamical behavior of the system for different initial conditions and temperatures. The temperature of one actuator is modified while the other remains constant at the reference temperature. Fig. 14 presents the phase space at different temperatures for the TSW-1 while TSW-2 temperature is T_0. The sum of the moments points up to three equilibrium points at $T_1 = T_0$, and the phase space

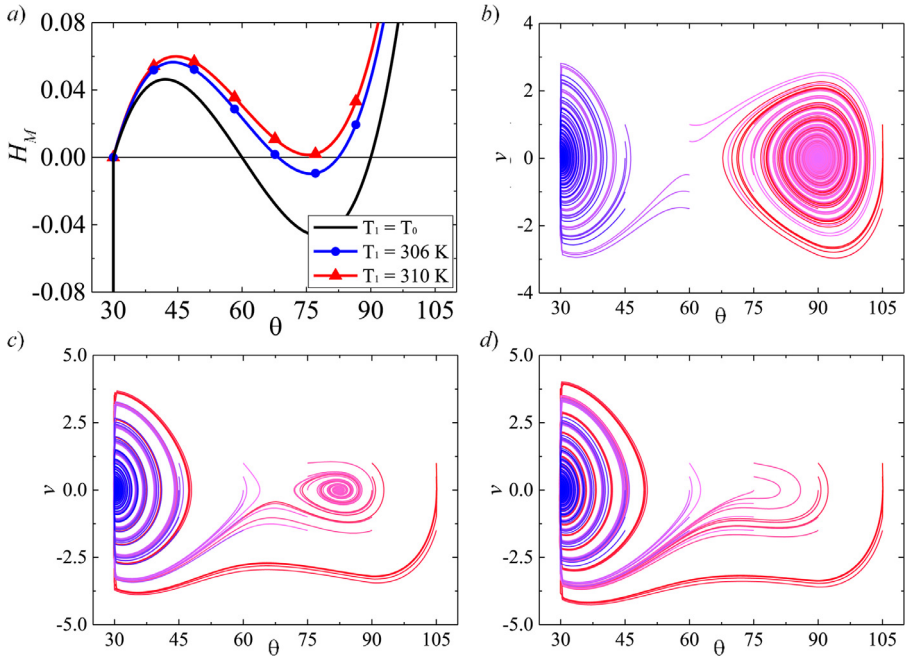

Fig. 14. Origami free vibration response at different temperatures with 6 elements ($n = 6$). (a) Sum of the moments at $T_2 = T_0$ and different values of T_1. (b) Phase space at $T_1 = T_0$. (c) Phase space at $T_1 = 306$ K. (d) Phase space at $T_1 = 310$ K.

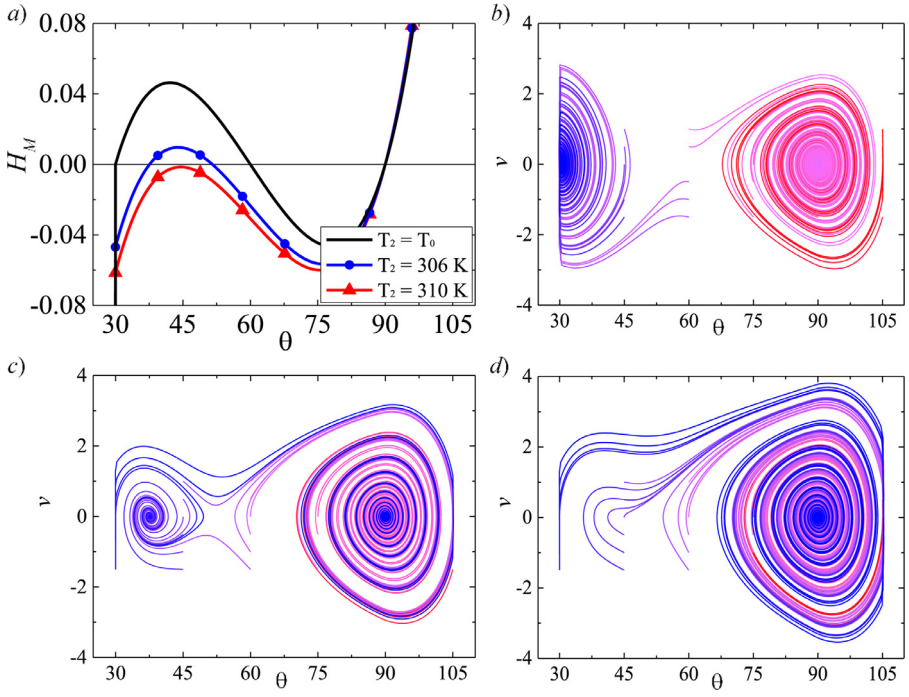

Fig. 15. Origami free vibration response at different temperatures with 6 elements ($n = 6$). (a) Sum of the moments at $T_1 = T_0$ and different values of T_2. (b) Phase space at $T_2 = T_0$. (c) Phase space at $T_2 = 306$ K. (d) Phase space at $T_2 = 310$ K.

shows that two of them are stable while the other one is unstable. By increasing the temperature T_1 ($T_1 = 306$ K), 30° remains a stable equilibrium point while the other stable equilibrium point is, now, smaller than 90° When $T_1 > T_A$ ($T_1 = 310$ K), only 30° is an equilibrium point, meaning that the structure admits only the closed configuration.

Fig. 15 presents the phase space at different temperatures for the TSW-2 while the temperature of the TSW-1 is T_0. By increasing the temperature T_2 ($T_2 = 306$ K), 90° remains a stable equilibrium point while the other stable equilibrium point is now, greater than 30° When $T_2 > T_A$ ($T_2 = 310$ K), only 90° is an equilibrium point, and the structure only admits an opened configuration. It is important to highlight that the origami-stent is initially in a reference configuration where the structure is closed ($\theta = 30°$). The opened configuration can be reached either by temperature variation or by imposing proper initial conditions, as one can see in Fig. 15-a (or Fig. 14-a). This reveals an initial condition dependence that is now investigated using different thermal loads.

From the reference condition, when temperature T_2 increases up to 310 K, the origami-stent opens (Fig. 16). System response presents an oscillation before reaching $\theta = 90°$ If the temperature T_2 decreases to T_0 again, the origami-stent remains in the opened configuration. By in-

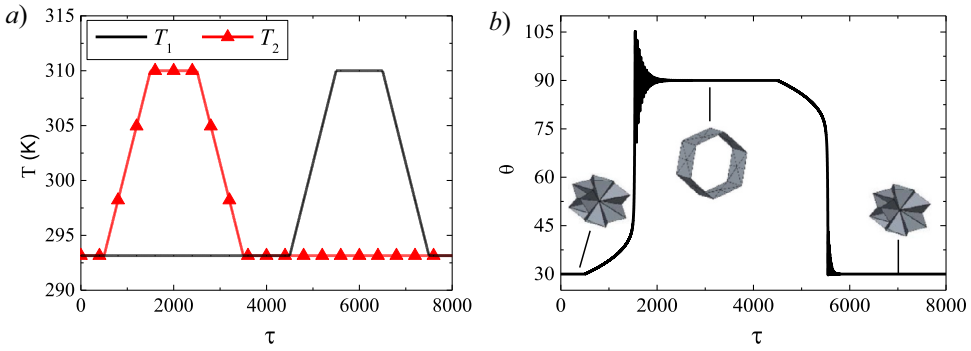

Fig. 16. Opening-closing process induced by temperature variations ($n=6$): (a) thermal load; (b) time history of the deployment angle θ.

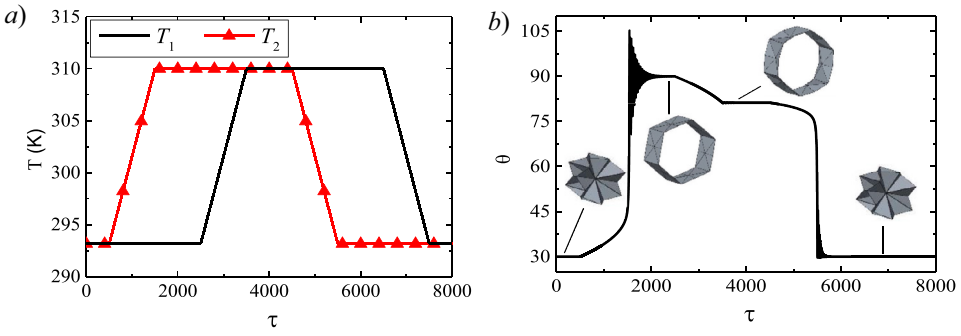

Fig. 17. Opening-closing process induced by temperature variations ($n=6$): (a) thermal load; (b) time history of the deployment angle θ.

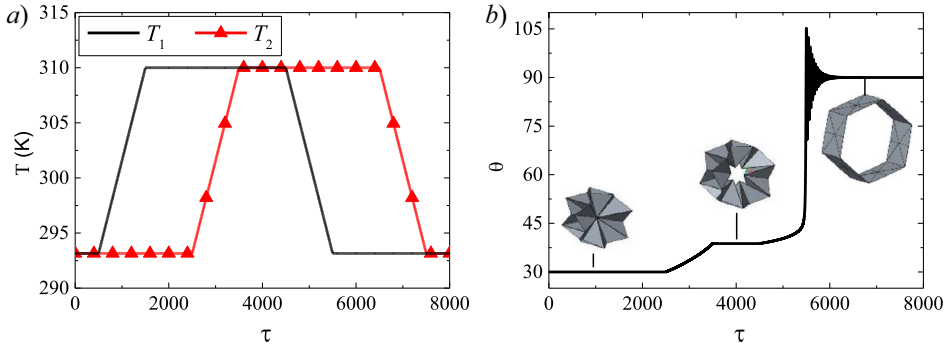

Fig. 18. Opening process induced by temperature variations ($n=6$): (a) thermal load; (b) time history of the deployment angle θ.

creasing temperature T_1, 90° is not an equilibrium point anymore and the origami-stent closes. By decreasing T_1 to T_0, the structure remains closed.

A different thermal loading is now investigated. By increasing T_2 up to 310 K and subsequently increasing T_1 up to 310 K (Fig. 17), the structure remains opened but not completely, since the equilibrium point is around 82° By decreasing the temperature T_2, the origami-stent closes and by decreasing T_1 there is no more changes.

In contrast, if T_1 is first increased (Fig. 18), there is no structure change. By increasing T_2 subsequently, there is a small increase of the angle θ and it stabilizes around 38° If T_1 decreases, the stent-origami opens and, subsequently, if T_2 decreases, it remains opened.

Equilibrium configuration small increase can be obtained increasing both temperatures T_1 and T_2 simultaneously as presented in Fig. 19. Note that the angle θ is changed to 38°

Until now, all simulations consider the same number of elements, $n=6$. The change of the number of elements can influence the dynamical response, which is now investigated. The first point that should be observed is that when n changes, the limit angles change; both θ_{min} and θ_{max} tend to reduce for greater values of n. For $n=6$, $\theta_{min}=30°$ and $\theta_{max}=105°$ For $n>6$, $\theta_{min}<30°$ and the origami is not completely closed at the reference condition and $\theta_{max}<105°$ Besides that, Fig. 9 shows that the amount of kinetic energy is larger for greatest values of n. Fig. 20 presents the origami response when temperature T_2 increases from the reference condition causing the opening of the origami. Different values of n are treated. Although the actuation response occurs at the same time, the stabilization takes more time to occur for origami with larger number of elements due to the greater amount of kinetic energy.

Since the origami system has strong temperature dependent behavior, it is important to evaluate the effect of thermal oscillations on system response. Figs. 21–23 present the influence of thermal oscillations on temperatures T_1 and T_2 considering $n=6$. Fig. 21 presents the opening process changing temperature T_2. Afterward, both temperatures oscillate at the opened configuration. A variation of temperature T_2 does not alter the response, but a variation of the temperature T_1 causes small oscillations. The TSW-2 is at a high temperature and 90° is a free-stress point (see Fig. 12) that does not change with the thermal variation. Based on that, the sum of system moments is not altered and, therefore, its equilibrium point does not change. However, the TSW-1 is at the ref-

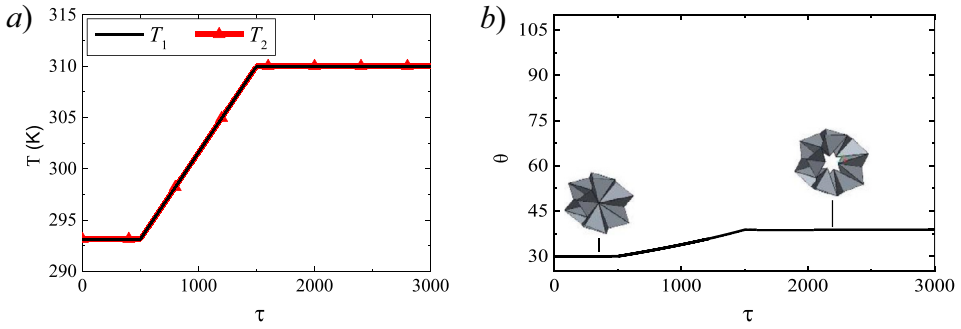

Fig. 19. Opening process induced by temperature variations ($n=6$): (a) thermal load; (b) time history of the deployment angle θ.

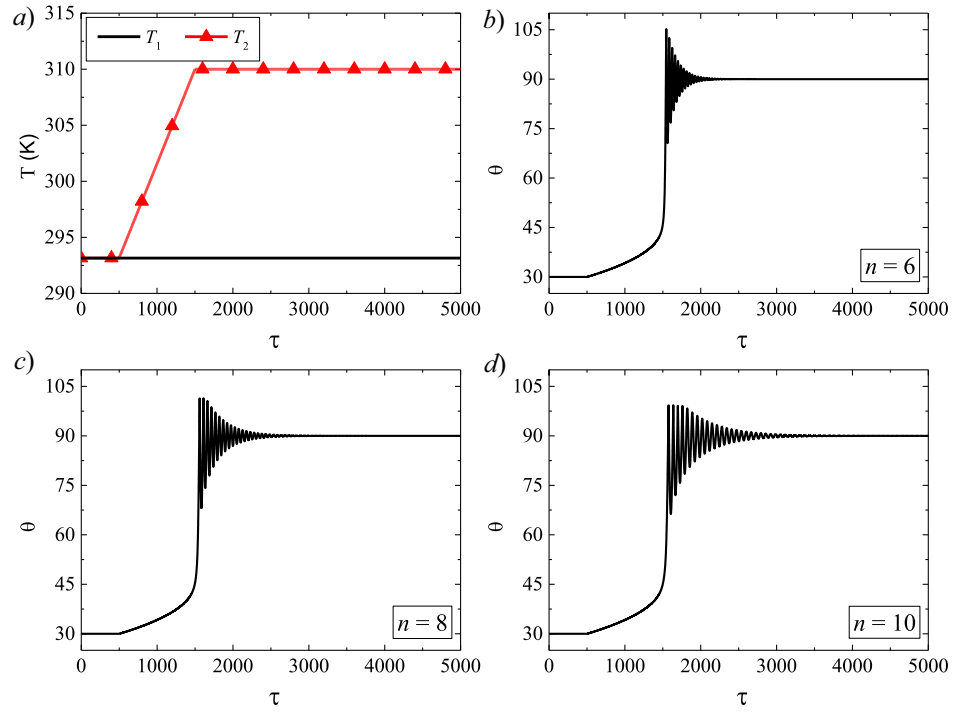

Fig. 20. Comparison of the opening process considering different values of the number of elements, n. (a) thermal load; time history of the deployment angle θ for: (b) $n=6$; (c) $n=8$; (d) $n=10$.

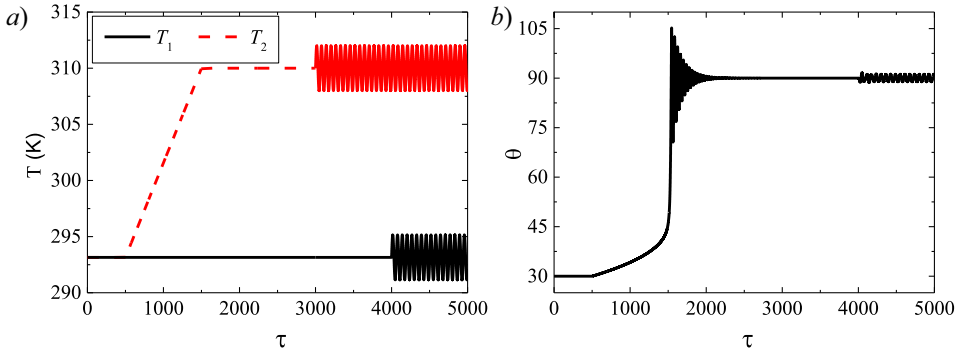

Fig. 21. Opening process with thermal oscillation ($n=6$): (a) thermal load ($\mu_T=2.0$ K and $\Omega_T=0.1$); (b) time history of the deployment angle θ.

erence temperature and thermal fluctuation alters the free-stress points, except the one at 30° Hence, the sum of the moments is altered and its equilibrium point oscillates while the temperature T_1 oscillates.

Fig. 22 shows a similar opening condition but with a situation where both T_1 and T_2 are increased. Under this assumption, a variation of temperature T_2 also induces oscillations and the origami response is a combination of both influences. Since both actuators have $T > T_A$, a variation of any actuator temperature is responsible to alter the sum of the moments of the system and, as a consequence, there is an oscillatory response. Besides, frequency thermal frequency phase is analyzed. It is noticeable that when actuator thermal variation is out of phase, the oscillatory response has higher amplitude.

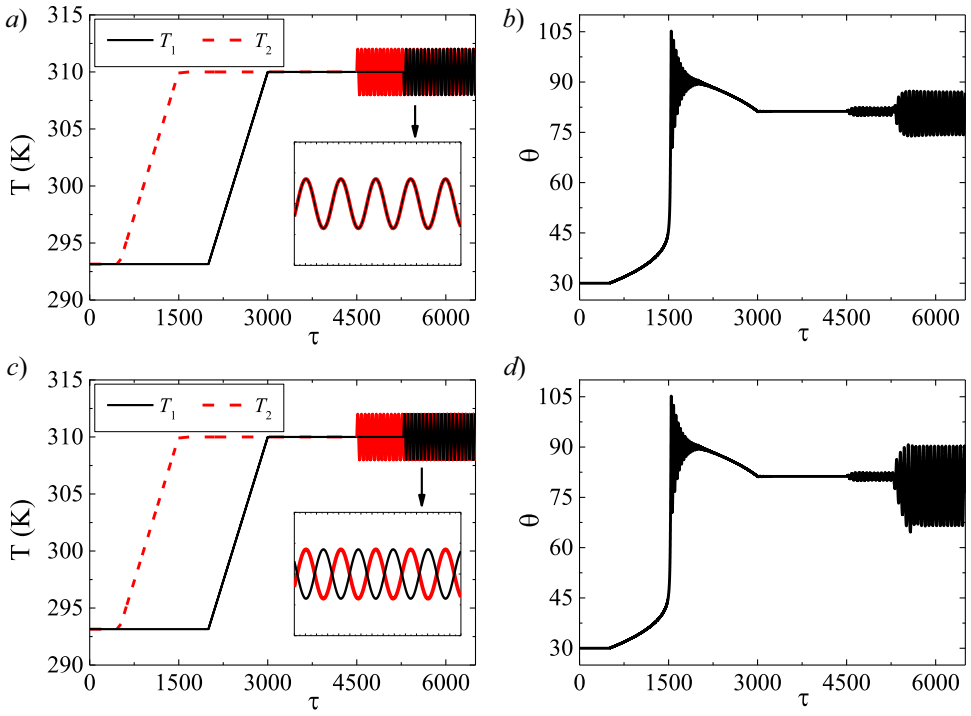

Fig. 22. Opening process with thermal oscillation ($n=6$): (a) and (c) thermal load ($\mu_T=2.0$ K and $\Omega_T=0.1$); (b) and (d) time history of the deployment angle θ.

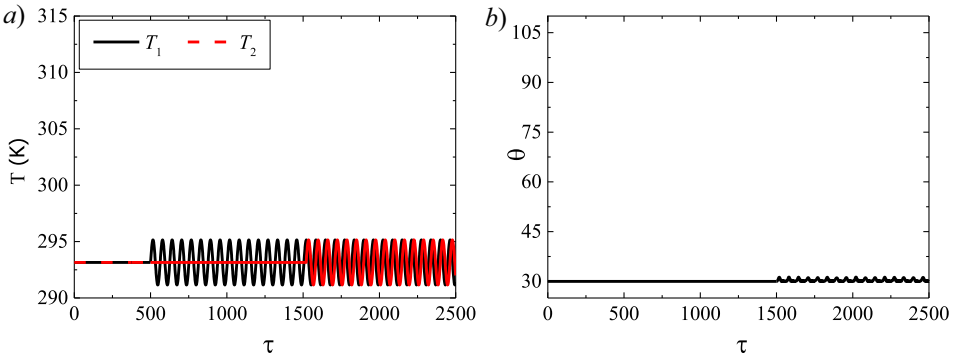

Fig. 23. Closed configuration with thermal oscillation ($n=6$). (a) Thermal load ($\mu_T=2.0$ K and $\Omega_T=0.1$); (b) time history of the deployment angle θ.

Fig. 23 presents a situation where both actuators have $T < T_A$, characterizing a closed configuration. Under this condition, only the variation of T_2 affects the dynamic response. In contrast of the case of Fig. 21, small fluctuation of T_1 does not alter actuator dynamical response since 30° is an actuator free-stress point (see Fig. 12) that does not change with a thermal variation. On the other hand, TSW-2 has 90° as a free-stress point that does not change, while the other points change with the temperature and, hence, thermal fluctuation changes the sum of the moments, affecting the system equilibrium point.

The influence of the number of elements in a case with thermal fluctuation is presented in Fig. 24. Note that the increase of the number of elements, n, tends to cause a greater change on system response.

4.2. Thermomechanical loadings

Thermomechanical loadings are now addressed in order to simulate some operational conditions of the origami-stent. Basically, opened configuration is of concern considering $T_1 = T_0$ and $T_2 = 310$ K. Under this condition, only 90° is an equilibrium point and an external force is applied. In order to establish a physical interpretation, the origami-stent system is assumed to represent human body stent. Under this assumption, the magnitude of the external force is compatible to the human body blood pressure. Hence, the dimensionless amplitude μ of the external force D_{ext} is in a range from 0.01 to 0.85, which is related to force of magnitude 10^{-3} N.

Initially, a global analysis is performed considering bifurcation diagrams that present a stroboscopic view of system dynamics under the slow quasi-static variation of parameter μ for $\Omega=0.30$ and different number of elements: $n=6$; $n=8$; $n=10$ (Fig. 25). Fig. 25-a considers $n=6$. Note that, for small force amplitudes, the system presents period-1 response until $\mu=0.143$. After that, a cloud of points suggests a chaotic response. By increasing the value of μ, the diagram shows other regions where the system response has a periodicity greater than 1. When $\mu=0.156$, bifurcations start from chaotic-like response to period-1 response. A period doubling can be noticed at $\mu=0.260$, nevertheless a period-1 response is predominant until $\mu=0.628$, where the system response becomes chaotic. Inside this chaotic region, there are some periodic windows, especially between $\mu=0.740$ and $\mu=0.781$.

By considering different number of elements, $n=8$ (Fig. 25-b) and $n=10$ (Fig. 25-c), it is noticeable that the increase of the number of elements tends to stretch the diagram and spread the kind of behavior over the values of μ. Note, for instance, that period-1 response for small

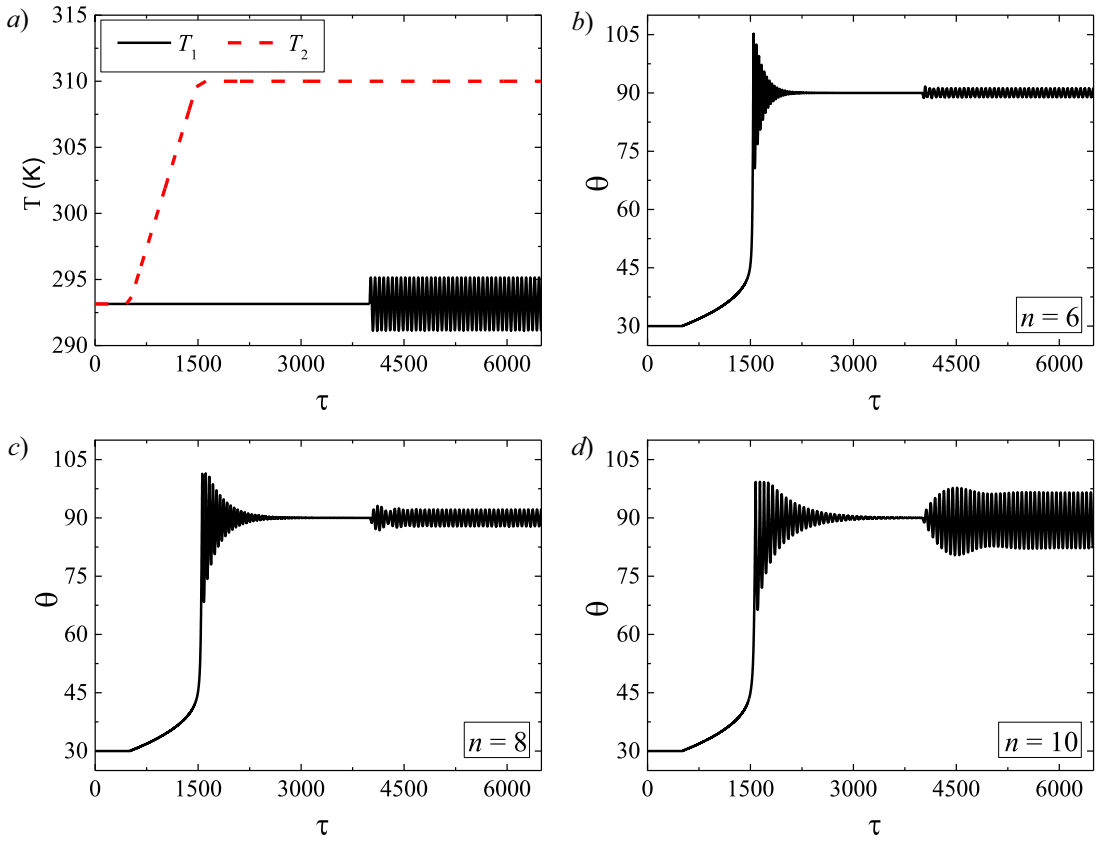

Fig. 24. Comparison of the opening process with thermal oscillation considering different values of the number of elements, *n*. (a) Thermal load; time history of the deployment angle θ for: (b) $n=6$: (c) $n=8$; (d) $n=10$.

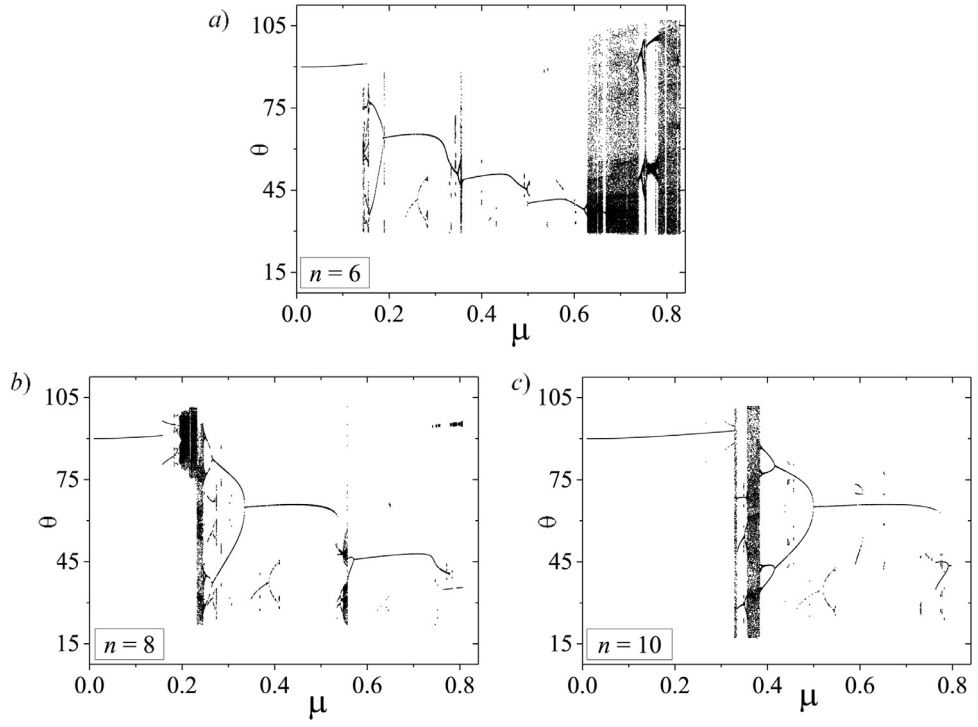

Fig. 25. Bifurcation diagrams varying excitation amplitude μ for different number of elements and a fixed frequency ($\Omega=0.30$): (a) $n=6$; (b) $n=8$; (c) $n=10$.

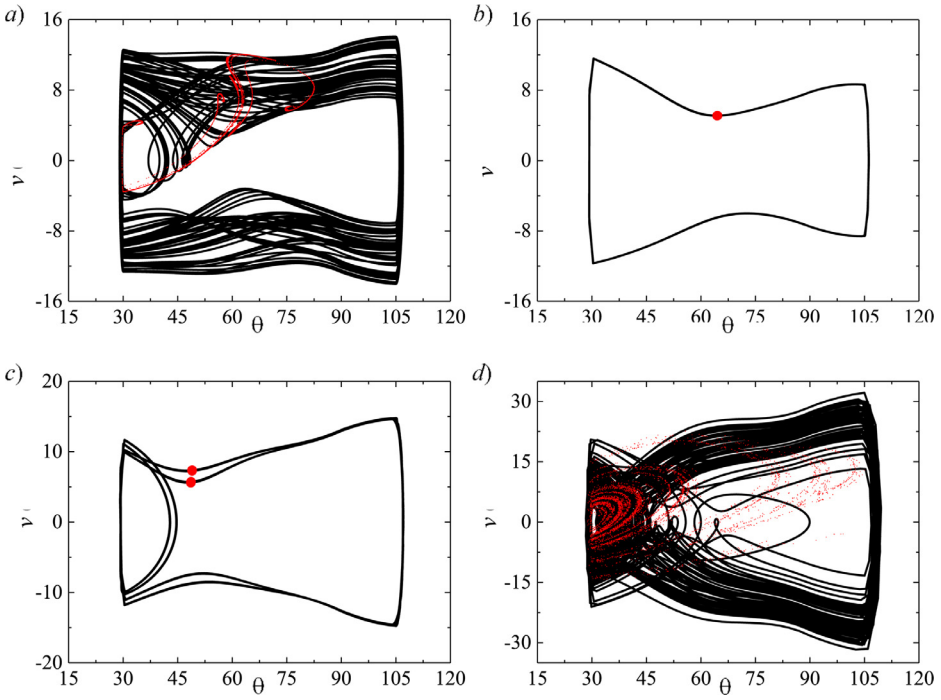

Fig. 26. Origami-stent response for $\Omega = 0.3$ and $n = 6$. Phase space (black lines) and Poincaré section (red points). (a) $\mu = 0.145$. (b) $\mu = 0.200$; (c) $\mu = 0.360$. (d) $\mu = 0.700$. (For interpretation of the references to color in this figure legend, the reader is referred to the web version of this article.)

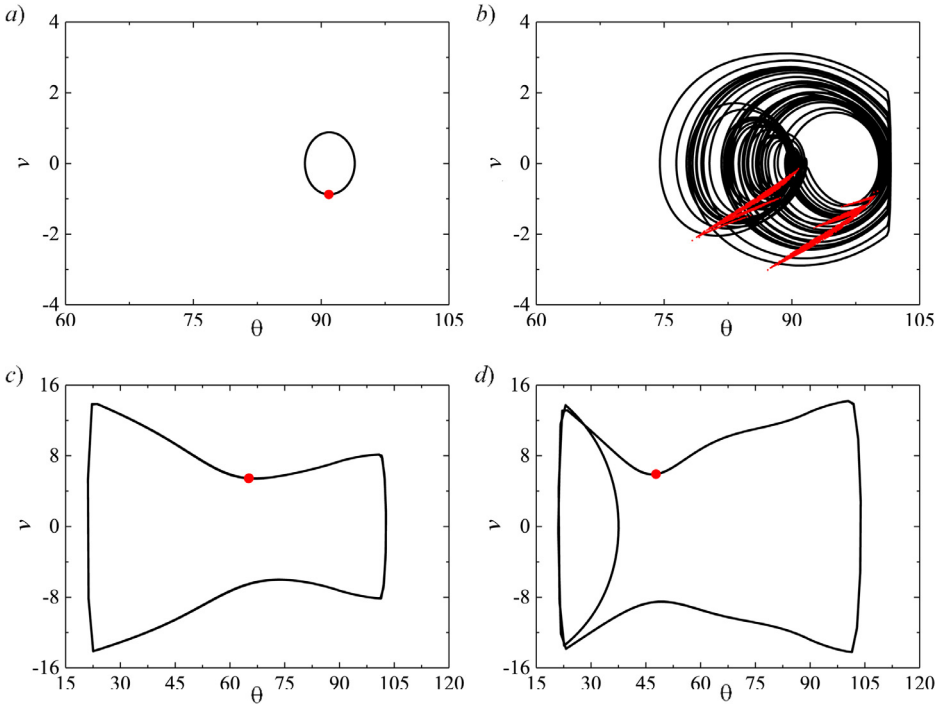

Fig. 27. Origami-stent response for $\Omega = 0.3$ and $n = 8$. Phase space (black lines) and Poincaré section (red points). (a) $\mu = 0.145$. (b) $\mu = 0.200$; (c) $\mu = 0.360$. (d) $\mu = 0.700$. (For interpretation of the references to color in this figure legend, the reader is referred to the web version of this article.)

amplitudes of the force finishes at $\mu = 0.143$ when $n = 6$ but at $\mu = 0.157$ when $n = 8$ and at $\mu = 0.308$ when $n = 10$. After the region of period-1 response, different bifurcation evolutions occur for each cell number. When $n = 6$, the cloud of points occurred immediately after the period-1 response. When $n = 8$, a period doubling takes place until the system response is quasi-periodic and then, the cloud of points takes place. When $n = 10$, a period doubling occurs then the cloud of points takes place. Subsequently, a periodic response window is noticed until there is a response sudden change suggesting a chaotic response. Afterward, a bifurcation from chaos to period-1 occurs.

Phase space and its respective Poincaré section are presented in Fig. 26 for different amplitudes of the external force taken from the bifurcation diagram of $n = 6$. In all these cases, the external force is great enough to push the origami to its physical limits, which is indicated by the straight lines at 30° and 105° For $\mu = 0.145$, a point inside the cloud of points region, a chaotic response occurs. By increasing values of μ,

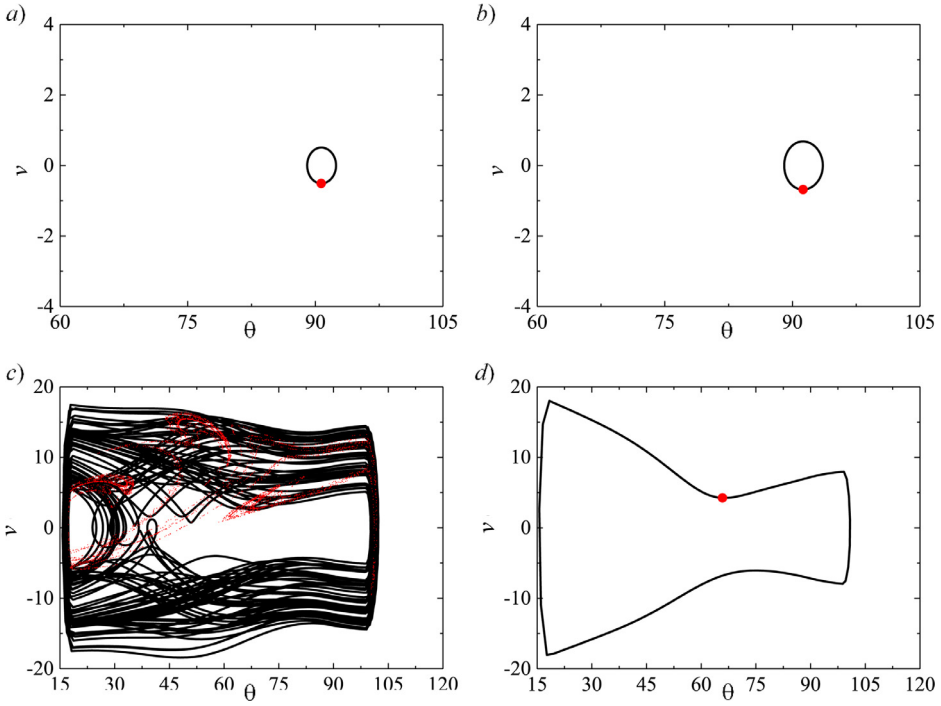

Fig. 28. Origami-stent response for $\Omega = 0.3$ and $n = 10$ elements. Phase space (black lines) and Poincaré section (red points). (a) $\mu = 0.145$. (b) $\mu = 0.200$; (c) $\mu = 0.360$. (d) $\mu = 0.700$. (For interpretation of the references to color in this figure legend, the reader is referred to the web version of this article.)

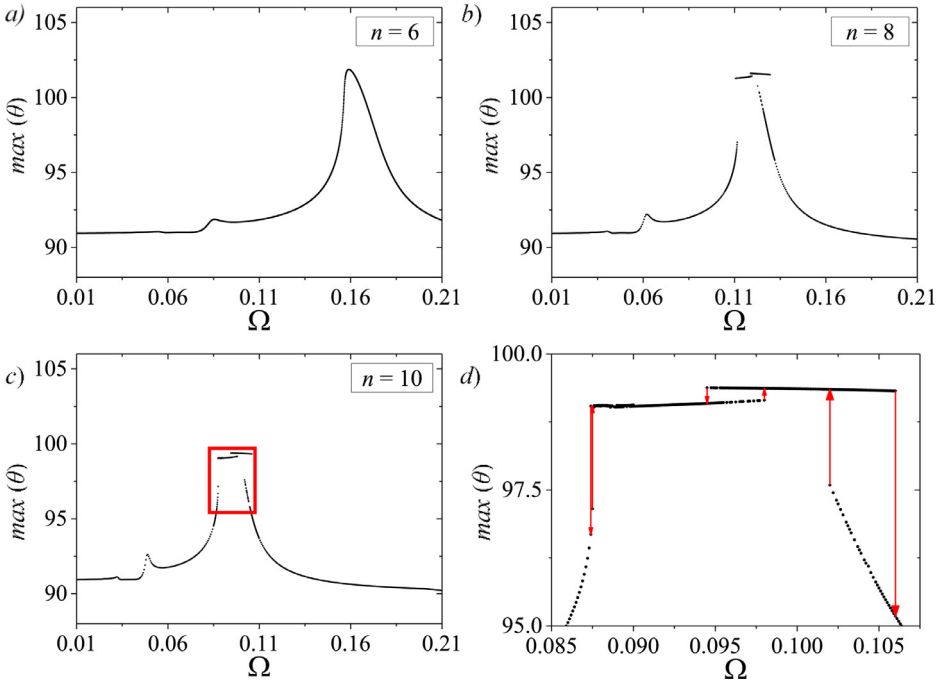

Fig. 29. Origami-stent frequency diagram for $\mu = 0.01$ and different number of elements: (a) $n = 6$; (b) $n = 8$; (c) $n = 10$; (d) enlargement of the resonance region for $n = 10$ elements showing dynamical jumps.

period-1 and period-2 responses are achieved for $\mu = 0.20$ and $\mu = 0.36$, respectively. A chaotic response is again obtained for $\mu = 0.70$.

The same results of Fig. 26, that considers $n = 6$, is now presented for $n = 8$, Fig. 27, and $n = 10$, Fig. 28. When $\mu = 0.145$ (Figs. 27-a and 28-a), the system oscillates around 90° with a period-1 response, without reaching the physical limits of the structure. When $\mu = 0.20$, there is a quasi-periodic response for $n = 8$ and, even if the system still oscillates around 90°, the upper physical limit is reached. In contrast, for $n = 10$, this increase of μ does not affect the system response substantially. On the other hand, when $\mu = 0.36$, the system response is periodic for $n = 8$, but chaotic for $n = 10$. When $\mu = 0.70$, a period-1 response is noticed.

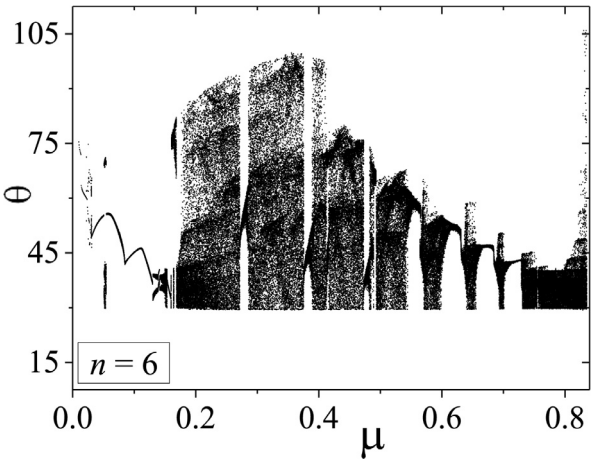

Fig. 30. Bifurcation diagram varying the excitation amplitude μ for $\Omega = 0.16$ and for $n = 6$.

Resonant condition is usually critical to system response. Concerning chaotic behavior, they can be induced more effectively close to this condition. In this regard, Fig. 29 presents the maximum amplitude of displacement under the variation of frequency Ω. For $n = 6$ (Fig. 29-a), it presents a typical resonant curve with maximum amplitude at $\Omega = 0.159$. It is also noticeable a small peak at $\Omega = 0.085$, related to constitutive nonlinearities. For $n = 8$ and $n = 10$, the peaks of maximum angle is shifted to the left and the flat region related to the maximum values is due to the maximum displacement constraints imposed by the origami physical limits. Besides, the smaller peak is more pronounceable. Furthermore, Fig. 29-d presents a zoom in Fig. 29-c where dynamical jumps for different frequencies are observed.

Fig. 30 shows the bifurcation diagram for $n = 6$ varying μ under resonant condition ($\Omega = 0.16$). Note that system response is predominantly chaotic indicating the influence of the resonant condition on system dynamics. Phase space and Poincaré section is presented in Fig. 31 for $\Omega = 0.16$ and $\mu = 0.20$. A chaotic-like response is observed presenting a strange attractor in Poincaré section.

5. Conclusions

This paper deals with the nonlinear dynamical analysis of an origami-stent actuated by shape memory alloys. A polynomial constitutive model is employed to describe the thermomechanical behavior of SMA actuators. Geometrical relations allow one to build a single degree of freedom system to analyze the system dynamics. This system has both constitutive and geometrical nonlinearities, presenting nonsmooth characteristics. Numerical simulations are carried out showing different thermomechanical loading situations representing operational conditions. Concerning thermal loadings, it is possible to identify that different configurations can be reached by changing the temperature of each actuator. Results are affected by the order of actuation. Moreover, thermal fluctuations can affect the system response depending on conditions. It depends on either the origami configuration or the actuator temperature. The number of cell elements interferes on the response stabilization time as well. An origami with more cell elements takes more time to stabilize, being more affected by thermal fluctuations. Thermomechanical loadings can produce complex responses including chaos. The number of cell elements is critical in order to define the system response. In general, the increase of the number of cell elements reduces chaotic regions. Furthermore, greater values of external force are needed to push the origami to reach its physical limits. Dynamical jumps are also observed on origami-stent dynamics.

Acknowledgments

The authors would like to acknowledge the support of the Brazilian Research Agencies CNPq, CAPES and FAPERJ. The Air Force Office of Scientific Research (AFOSR - Grant FA9550-16-0381) is also acknowledged.

Appendix

Origami-stent equations of motion are related to complex functions that express geometric relations. Kinetic energy definition (Eq. (23)) is described on the global coordinate frame F, using transformation matrix. Therefore, consider that kinetic energy, Eq. (22), can be written as follows:

$$E = g(\theta)\dot{\theta}^2$$

Applying this equation in the left hand side of the Lagrange's equation (Eq. (28)):

$$\frac{\partial}{\partial t}\left(\frac{\partial E}{\partial \dot{\theta}}\right) = \frac{\partial}{\partial t}\left(\frac{\partial}{\partial \dot{\theta}}^{g(\theta)\dot{\theta}^2}\right) = 2g(\theta)\ddot{\theta} + 2\dot{\theta}\frac{\partial}{\partial t}^{g(\theta)} = 2g(\theta)\ddot{\theta} + 2\dot{\theta}^2\frac{\partial}{\partial \theta}^{g(\theta)}$$

$$\frac{\partial E}{\partial \theta} = \frac{\partial}{\partial \theta}^{\left(g(\theta)\dot{\theta}^2\right)} = \dot{\theta}^2\frac{\partial}{\partial \theta}^{g(\theta)}$$

Combining the terms with $\ddot{\theta}$ and $\dot{\theta}^2$, two others functions, $g_1(\theta)$ and $g_2(\theta)$, are defined:

$$\frac{\partial}{\partial t}\left(\frac{\partial E}{\partial \dot{\theta}}\right) - \frac{\partial E}{\partial \theta} = 2g(\theta)\ddot{\theta} + \dot{\theta}^2\frac{\partial}{\partial \theta}^{g(\theta)} = g_1(\theta)\ddot{\theta} + g_2(\theta)\dot{\theta}^2$$

Therefore, $g_1(\theta) = 2g(\theta)$ and $g_2(\theta) = \partial g(\theta)/\partial\theta$. The equation $g(\theta)$ is presented in the sequence, where $(\,)' = \partial(\,)/\partial\theta$, reminding that φ and

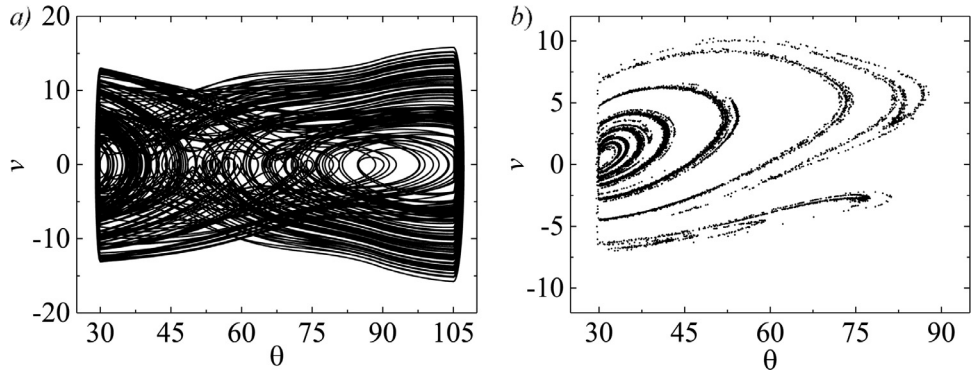

Fig. 31. Chaotic response for $\mu = 0.20$, $\Omega = 0.16$ and $n = 6$. (a) Phase space. (b) Poincaré section.

β are functions of θ:

$$
\begin{aligned}
g(\theta) = {} & \tfrac{1}{2} m_1 L^2 \Big\{ \tfrac{1}{9}\beta'^2 \cos^2(\beta) \\
& \left[-\tfrac{1}{3}\varphi' \sin(\varphi)\cos(\beta) - \tfrac{1}{3}\beta' \cos(\varphi)\sin(\beta) + \frac{2}{3\tan(\alpha_0)}\varphi' \cos(\varphi) \right]^2 \\
& + \left[-\tfrac{1}{3}\varphi' \cos(\varphi)\cos(\beta) + \tfrac{1}{3}\beta' \sin(\varphi)\sin(\beta) - \frac{2}{3\tan(\alpha_0)}\varphi' \sin(\varphi) + R_i' \right]^2 \\
& + \Big[\varphi'^2 \Big(\Big(\tfrac{1}{6} + \frac{1}{2\tan^2(\alpha_0)} \Big) \cos^2(\beta) + \frac{1}{2\tan^2(\alpha_0)} \sin(\beta) + R_i'^2 \\
& + 2R_i' \Big(-\tfrac{1}{3}\sin(\varphi)\cos(\beta) + \frac{2}{3\tan(\alpha_0)}\cos(\varphi) \Big) \Big) \\
& + \beta' \sin(\varphi) \Big(\cos(\varphi) \Big(-\cos(\beta)\sin(\beta) \Big(\tfrac{1}{6} + \frac{1}{2\tan^2(\alpha_0)} \Big) + \frac{1}{2\tan^2(\alpha_0)} \cos(\beta)\sin(\beta) \Big) \\
& - \frac{1}{4\tan(\alpha_0)} \sin(\beta)\sin(\varphi) \Big) \\
& + \beta' \cos(\varphi) \Big(-\sin(\varphi) \Big(-\sin(\beta)\cos(\beta) \Big(\tfrac{1}{6} + \frac{1}{2\tan^2(\alpha_0)} \Big) + \frac{1}{2\tan^2(\alpha_0)} \sin(\beta)\cos(\beta) \Big) \\
& - \frac{1}{4\tan(\alpha_0)} \sin(\beta)\cos(\varphi) - \tfrac{1}{3} R_i' \sin(\beta) \Big) \Big] \\
& + \tfrac{1}{2}\beta' \sin(\varphi) \Big[\varphi' \Big(\cos(\varphi) \Big(-\sin(\beta)\cos(\beta) \Big(\tfrac{1}{6} + \frac{1}{2\tan^2(\alpha_0)} \Big) + \frac{1}{2\tan^2(\alpha_0)} \sin(\beta)\cos(\beta) \Big) \\
& - \frac{1}{4\tan(\alpha_0)} \sin(\beta)\sin(\varphi) \Big) \\
& + \beta' \sin(\varphi) \Big(\cos(\varphi) \Big(\cos(\varphi) \Big(\sin^2(\beta) \Big(\tfrac{1}{6} + \frac{1}{2\tan^2(\alpha_0)} \Big) \\
& + \frac{1}{2\tan^2(\alpha_0)} \cos^2(\beta) \Big) - \frac{1}{4\tan(\alpha_0)} \sin(\varphi)\sin(\beta) \Big) \\
& + \Big(-\frac{1}{4\tan(\alpha_0)} \cos(\varphi)\cos(\beta) + \tfrac{1}{6}\sin(\varphi) \Big) \sin(\varphi) \\
& + \Big(R_i'^2 + 2R_i' \Big(-\tfrac{1}{3}\sin(\varphi)\cos(\beta) + \frac{2}{3\tan(\alpha_0)}\cos(\varphi) \Big) \Big) \Big) \\
& + \beta' \cos(\varphi) \Big(\cos(\varphi) \Big(-\sin(\varphi) \Big(\sin^2(\beta) \Big(\tfrac{1}{6} + \frac{1}{2\tan^2(\alpha_0)} \Big) + \frac{1}{2\tan^2(\alpha_0)} \cos^2(\beta) \Big) \\
& - \frac{1}{4\tan(\alpha_0)} \cos(\varphi)\cos(\beta) \Big) + \sin(\varphi) \Big(\frac{1}{4\tan(\alpha_0)} \sin(\varphi)\cos(\beta) + \tfrac{1}{6}\cos(\varphi) \Big) \\
& - R_i' \Big(\tfrac{1}{3}\cos(\varphi)\cos(\beta) + \frac{2}{3\tan(\alpha_0)}\sin(\varphi) \Big) \Big) \Big] \\
& + \tfrac{1}{2}\beta' \cos(\varphi) \Big[\varphi' \Big(-\sin(\varphi) \Big(-\sin(\beta)\cos(\beta) \Big(\tfrac{1}{6} + \frac{1}{2\tan^2(\alpha_0)} \Big) \\
& + \frac{1}{2\tan^2(\alpha_0)} \sin(\beta)\cos(\beta) \Big) - \frac{1}{4\tan(\alpha_0)} \sin(\beta)\cos(\varphi) - \tfrac{1}{3} R_i' \sin(\beta) \Big) \\
& + \beta' \sin(\varphi) \Big(-\sin(\varphi) \Big(\cos(\varphi) \Big(\sin^2(\beta) \Big(\tfrac{1}{6} + \frac{1}{2\tan^2(\alpha_0)} \Big) \\
& + \frac{1}{2\tan^2(\alpha_0)} \cos^2(\beta) \Big) - \frac{1}{4\tan(\alpha_0)} \sin(\varphi)\cos(\beta) \Big) \\
& + \cos(\varphi) \Big(-\frac{1}{4\tan(\alpha_0)} \cos(\varphi)\cos(\beta) + \tfrac{1}{6}\sin(\varphi) \Big) \\
& - R_i' \Big(\tfrac{1}{3}\cos(\varphi)\cos(\beta) + \frac{2}{3\tan(\alpha_0)}\sin(\varphi) \Big) \Big) \\
& + \beta' \cos(\varphi) \Big(-\sin(\varphi) \Big(-\sin(\varphi) \Big(\sin^2(\beta) \Big(\tfrac{1}{6} + \frac{1}{2\tan^2(\alpha_0)} \Big) + \frac{1}{2\tan^2(\alpha_0)} \cos^2(\beta) \Big) \\
& - \frac{1}{4\tan(\alpha_0)} \cos(\varphi)\cos(\beta) \Big) + \cos(\varphi) \Big(\frac{1}{4\tan(\alpha_0)} \sin(\varphi)\cos(\beta) + \tfrac{1}{6}\cos(\varphi) \Big) \Big) \Big] \Big\} \\
& + \tfrac{1}{2} m_2 L^2 \Big\{ \tfrac{1}{4} + \tfrac{4}{9}\cos^2(\theta) + \Big(\tfrac{1}{3}\sin(\theta) + \frac{\cos(\theta)}{\tan(\alpha)} \Big)^2 + \tfrac{1}{2} \Big(R_i'^2 + \tfrac{4}{3} R_i' \cos(\theta) \Big) \Big\}
\end{aligned}
$$

References

[1] Aguiar RA, Savi MA, Pacheco PM. Experimental and numerical investigations of shape memory alloy helical springs. Smart Mater Struct 2010;19(2):025008.

[2] Enemark S, Santos IF, Savi MA. Modelling, characterisation and uncertainties of stabilised pseudoelastic shape memory alloy helical springs. J Intell Mater Syst Struct 2016 doi:10.1177/1045389X16635845.

[3] Falk F. Model free energy, mechanics, and thermodynamics of shape memory alloys. Acta Metall 1980;28(12):1773–80.

[4] Fei LJ, Sujan D. Origami Theory and its Applications: A Literature Review. In: Tang FE, et al., editors. 7th Curtin University Conference (CUTSE) Engineering Goes Green, Nov 6–7 2012. Sarawak, Malaysia: Curtin University School of Engineering; 2012. p. 336–40.

[5] Fonseca LM, Rodrigues GV, Savi MA, Paiva A. Nonlinear dynamics of an origami structure coupled to smart materials. In: Proceedings of the sixth international conference on nonlinear science and complexity (NSC), São Paulo, Brazil; 2016.

[6] Hanna BH, Lund JM, Lang RJ, Magleby SP, Howell LL. Waterbomb base: a symmetric single-vertex bistable origami mechanism. Smart Mater Struct 2014;23(9):094009.

[7] Kim SR, Lee DY, Koh JS, Cho KJ. Fast, compact, and lightweight shape-shifting system composed of distributed self-folding origami modules. In: Proceedings of the IEEE international conference on robotics and automation. IEEE; 2016. p. 4969–74.

[8] Koh JS, Cho KJ. Omega-shaped inchworm-inspired crawling robot with large-index-and-pitch (LIP) SMA spring actuators. IEEE/ASME Trans Mechatron 2013;18(2):419–29.

[9] Koh JS, Kim SR, Cho KJ. Self-folding origami using torsion shape memory alloy wire actuators. In: Proceedings of the ASME international design engineering technical conferences and computers and information in engineering conference; 2014 V05BT08A043–V05BT08A043.

[10] Kuribayashi K. A novel foldable stent graft. University of Oxford); 2004.

[11] Kuribayashi K, Tsuchiya K, You Z, Tomus D, Umemoto M, Ito T, et al. Self-deployable origami stent grafts as a biomedical application of Ni-rich TiNi shape memory alloy foil. Mater Sci Eng A 2006;419(1):131–7.

[12] Le PH, Molina J, Hirai S. Application of Japanese origami ball for floating multirotor aerial robot. Int J Mech Aerosp Ind Mechatron Manuf Eng 2014;8(10):1747–50 World Academy of Science, Engineering and Technology.

[13] Lee D, Kim J, Kim SR, Koh JS, Cho KJ. The deformable wheel robot using magic-ball origami structure. In: Proceedings of the ASME international design engineering technical conferences and computers and information in engineering conference; 2013.

[14] Ma J, You Z. Modelling of the waterbomb origami pattern and its applications. In: Proceedings of the international design and engineering technical conferences and computers and information in engineering conference, Buffalo, NY. ASME; 2014.

[15] Miura K. Map fold a la Miura style, its physical characteristics and application to the space science. In: Takaki R, editor. Research of pattern formation. Tokyo: KTK Scientific Publishers; 1994. p. 77–90.

[16] Peraza-Hernandez EA, Hartl DJ, Malak RJ, Lagoudas DC. Origami-inspired active structures: a synthesis and review. Smart Mater Struct 2014;23:094001.

[17] Pesenti M, Masera G, Fiorito F, Sauchelli M. Kinetic solar skin: a responsive folding technique. Energy Proc 2015;70:661–72.

[18] Salerno M, Zhang K, Menciassi A, Dai JS. A Novel 4-DOFs origami enabled, SMA actuated, robotic end-effector for minimally invasive surgery. In: Proceedings of the IEEE International Conference on Robotics and Automation (ICRA2014); 2014. p. 2844–9.

[19] Savi MA, Pacheco PMLC. Chaos and hyperchaos in shape memory systems. Int J Bifur Chaos 2002;12(3):645–57.